Hindawi
Journal of Nanomaterials
Volume 2019, Article ID 8936095, 9 pages
https://doi.org/10.1155/2019/8936095

Research Article

Highly Sensitive Detection of Dopamine at Ionic Liquid Functionalized RGO/ZIF-8 Nanocomposite-Modified Electrode

Lei Cheng, Youjun Fan, Xingcan Shen, and Hong Liang

State Key Laboratory for Chemistry and Molecular Engineering of Medicinal Resources, School of Chemistry and Pharmaceutical Science, Guangxi Normal University, Guilin 541004, China

Correspondence should be addressed to Lei Cheng; chenglei@mailbox.gxnu.edu.cn, Xingcan Shen; xcshen@mailbox.gxnu.edu.cn, and Hong Liang; hliang@gxnu.edu.cn

Received 28 April 2019; Accepted 11 July 2019; Published 25 August 2019

Guest Editor: Laijun Liu

A hybrid and hierarchical nanocomposite was successfully prepared by the growth of zeolitic imidazolate framework-8 (ZIF-8) on the template of ionic liquid (IL, [Bmim][BF_4]) functionalized reduced graphene oxide (IL-RGO). The structure and morphology of the IL-RGO/ZIF-8 nanocomposite were characterized by X-ray diffraction (XRD), scanning electron microscopy (SEM), Fourier transform infrared spectrometer (FTIR), and Raman spectroscopy. The results showed that RGO sheets were refrained from restacking by IL, and ZIF-8 nanoparticles grew well on the surface of IL-RGO. Owing to the synergistic effect from large surface area and excellent electrocatalytic activity of ZIF-8 and great electrical conductivity of IL-RGO, a highly sensitive sensor for dopamine (DA) can be obtained. IL-RGO/ZIF-8-modified electrode exhibits good electrocatalytic activity and electroconductive properties towards DA which were investigated by cyclic voltammetry (CV), differential pulse voltammetry (DPV), and electrochemical impedance spectroscopy (EIS). Compared with bare or IL-RGO-modified electrodes, the IL-RGO/ZIF-8-modified electrode effectively depressed the oxidation overpotential of DA. The linear response range of DA was from 1.0×10^{-7} to 1.0×10^{-4} mol/L with a low detection of limit 3.5×10^{-8} mol/L. In addition, the sensor was shown to provide satisfactory stability for the determination of DA.

1. Introduction

As a message transmission medium between neurons and the brain, dopamine (DA) plays an important role as a neurotransmitter in mammalian central nervous systems [1, 2]. Several neurological illnesses could be related to an abnormal dopaminergic neuron process [3]. As a result, the clinical analysis needs an accurate, sensitive, and rapid determination of DA. Many methods, such as chemiluminescence [4], liquid chromatography [5, 6], capillary electrophoresis [7], and fluorescence [8], were proposed for detecting DA. Compared with them, the electrochemical method shows lower cost of instrument and operation, faster response, and higher accuracy [9].

Zeolitic imidazolate frameworks (ZIF) have ordered porous structure, constructed from metal ions and organic ligands, and are characterized by micropore size, high porosity, and large surface areas. ZIF-8 is one of the most interesting materials in the ZIF family, which is considered as a promising substrate for constructing electrochemical sensors [10, 11]. Ma et al. prepared an electrochemical biosensor based on ZIF-8 [12]; unfortunately, the conductivity of ZIF-8 is too poor and depresses the performance of the electrodes. Later, many researchers paid more attention to improve the conductivity of MOF-based composites with different conductive materials, such as metal nanoparticles [13, 14], organic polymers [15], and carbon [16, 17]. Based on excellent thermal, chemical, and mechanical stability, especially the exceptional electron transfer rate and superior electronic conductivity, graphene is widely used in sensing and biosensing [18]. Kinds of biomarker including glucose, hydrogen peroxide, dopamine, uric acid, ascorbic acid, and cancer markers have been detected based on graphene [19, 20]. The electrochemical determination performance was enhanced due to ultrafast electron transfer between the nanocomposite and electrode, which was caused by

the introduction of graphene. Kim et al. constructed a graphene/ZIF-8 composite by growing ZIF-8 crystal on graphene [21] to create fast mass transfer and high conductivity. Yu et al. prepared a hierarchical and hybrid nanocomposite of RGO/ZIF-8 which possesses high sensitivity for the determination of DA [22]. However, due to the high specific surface area of graphene, it is easy to form irreversible agglomerates or even restack through *van der Waals* interaction and π-π stacking [23]. As a result, it needs to be added much RGO to obtain good performance for the composite. It is reported that ionic liquid (IL) could prevent aggregation due to its wide solubility and created surface charge [24]. In addition, IL has a large electrochemical window up to 4 V, making it suitable for detecting various redox enzymes as electrochemical sensors and biosensors [25–27]. Therefore, the efficient direct electron transfer could be facilitated with the combination of IL and graphene.

In this work, nanocomposite IL-RGO/ZIF-8 (ionic liquid functionalized reduced graphene oxide/zeolitic imidazolate framework-8) was prepared by the growth of ZIF-8 on a small quantity of IL-RGO template. Crystal structure and morphology of the composite were identified by XRD and SEM, respectively. The prepared composite was coated on a glass carbon electrode (GCE) to fabricate a sensor for detecting DA. The electrochemical performance for DA detection is enhanced owing to the synergistic effect of ZIF-8 with large surface area and order porous structure and IL-RGO with high electronic conductivity.

2. Materials and Methods

2.1. Chemicals and Materials. Ionic liquid functionalized reduced graphene oxide (IL-RGO) was prepared according to Shao's method [28]. $Zn(CH_3COO)_2{\cdot}2H_2O$, 2-methylimidazole (Hmim), and dopamine (DA) were provided from Aladdin Reagent Co. Ltd. (Shanghai, China). H_2SO_4, $NaNO_3$, H_2O_2, hydrazine, 1-butyl-3-methylimidazolium tetrafluoroborate ([Bmim][BF_4]), and ethanol were obtained from Sinopharm Chemical Reagent Co. Ltd. Phosphate buffer solutions (PBS) with different pH values were prepared by mixing 0.02 M NaCl, $NaH_2PO_4{\cdot}2H_2O$, and $Na_2HPO_4{\cdot}12H_2O$. All chemicals were of analytical grade and used without further purification. Doubly distilled water (DDW) was used in these experiments.

2.2. Apparatus. The phase structure of ZIF-8 was identified by X-ray diffraction (XRD) on a Bruker D8-Advance diffractometer (Germany) using Cu $K\alpha$ radiation, $\lambda = 1.5415$ Å. Morphology of ZIF-8 and relative composites was observed by scanning electron microscopy (SEM, Philips-FEI, Netherlands). The bond vibration characterizations were investigated by Fourier transform infrared spectrometer (FTIR) (Perkin Elmer System 2000) and micro Raman spectroscopy (Renishaw-InVia, UK). Nitrogen adsorption-desorption isotherms were carried out using a volumetric adsorption analyzer (Bei Shi De 3H-2000PS4) at liquid nitrogen temperature (77 K). The surface area of the composites was determined by the Brunauer-Emmett-Teller (BET) method. Cyclic voltammetry (CV) and differential pulse voltammetry (DPV) were carried out on an electrochemical workstation (Parstat 3000A, American) with a conventional three-electrode system. An Ag/AgCl electrode [Ag/AgCl, KCl (sat′d)] was used as the reference electrode, a platinum plate as the auxiliary electrode, and glassy carbon electrodes (GCE) as the working electrode.

2.3. Preparation of ZIF-8 and IL-RGO/ZIF-8 Nanocomposite. An aqueous method for preparing ZIF-8 was employed as shown in literature [29]. And the preparation of IL-RGO/-ZIF-8 nanocomposite was as follows: first, 0.134 g of $Zn(CH_3COO)_2{\cdot}2H_2O$ and 5.3333 g of Hmim were dissolved in 15 mL and 25 mL of DDW, respectively. Then, 28 μL, 56 μL, and 84 μL of IL-RGO suspension (corresponding to 0.05 wt%, 0.10 wt%, and 0.15 wt%, respectively, for the production ZIF-8, assigned as IL-RGO(1)/ZIF-8, IL-RGO(2)/ZIF-8, and IL-RGO(3)/ZIF-8) were dropped into the $Zn(CH_3COO)_2$ aqueous solution with vigorous stirring for 3 min. Afterwards, the Hmim solution was added into the $Zn(CH_3COO)_2$ solution with vigorous stirring for 5 min. The mixture kept quietly maturing for 48 h. Then, the product was collected by centrifugal separation at 5000 rpm for 10 min and washed with DDW for three times repeatedly. Finally, the product was dried at 60°C for 48 h under vacuum.

2.4. Preparation of IL-RGO/ZIF-8-Modified Electrode. Bare GCE was polished with 50 nm alumina slurry and rinsed ultrasonically in DDW for 1 min, then dried by N_2. The IL-RGO/ZIF-8 was ultrasonically dispersed in DDW with the concentration of 1.0 mg mL^{-1}. Then, 10 μL of IL-RGO/ZIF-8 nanocomposite dispersion was dropped on the polished GCE surface and dried at room temperature to obtain the IL-RGO/ZIF-8-modified GCE (IL-RGO/ZIF-8/GCE). In addition, only ZIF-8-modified GCE (ZIF-8/GCE) and IL-RGO-modified GCE (IL-RGO/GCE) were prepared in the same way for comparison.

3. Results and Discussion

3.1. Characterization of IL-RGO/ZIF-8 Nanocomposite. The morphology of the nanocomposite was carried out by SEM. Smooth and flat sheets without wrinkles and noticeable pore in the rigid structure are observed in the image of IL-RGO as shown in Figure 1(a). It suggests that the aggregation of the RGO is prevented by ionic liquid due to its wide solubility and created surface charge. Pristine ZIF-8 crystals can be seen in Figure 2(b); it displays tightly distributed and homogeneous nanoparticles with hexagonal morphology. The average particle size is approximately 200 nm. With the increased contents of IL-RGO, the morphology of ZIF-8 crystals in IL-RGO/ZIF-8 nanocomposites is identical with the pristine ZIF-8, while the particle size increases slightly to 320 nm for IL-RGO(1)/ZIF-8 (Figure 1(c)) and then reduces to 120 nm for IL-RGO(2)/ZIF-8 and IL-RGO(3)/-ZIF-8 (Figures 1(d) and 1(e)). The increase of size of ZIF-8 on IL-RGO could associate with the nucleating center of ZIF-8 provided by IL-RGO, while the decrease may be

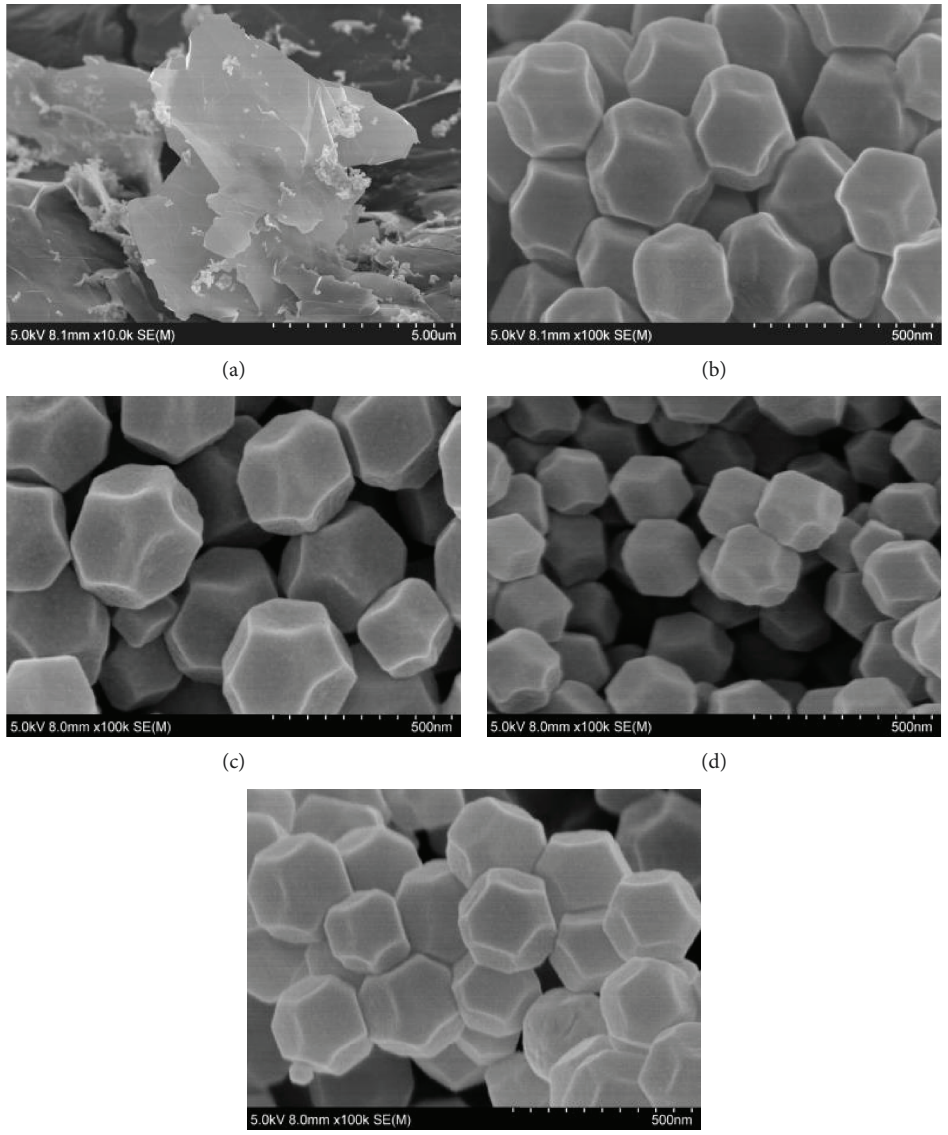

Figure 1: SEM images of (a) IL-RGO, (b) ZIF-8, (c) IL-RGO(1)/ZIF-8, (d) IL-RGO(2)/ZIF-8, and (e) IL-RGO(3)/ZIF-8.

contributed to the fact that (1) the 2D IL-RGO sheet restrains the free growth of ZIF-8 in the 3D direction and (2) the created surface charge on IL-RGO provides more nucleation centers for ZIF-8.

The XRD patterns of IL-RGO, ZIF-8, and IL-RGO/-ZIF-8 nanocomposites are shown in Figure 2(a). The Bragg reflections of ZIF-8 are identified well with the previous report [30–33]. It suggests that the pure ZIF-8 phase is successfully obtained. According to XRD patterns of the ZIF-8 and IL-RGO/ZIF-8 composites, the same Bragg reflections indicate that IL-RGO does not destroy the crystalline structure of ZIF-8. However, no characteristic peak of IL-RGO is presented in the patterns of the nanocomposites because of a low content of IL-RGO. On the other hand, the reflection (420) of ZIF-8 is the same angle (2theta ~23.5°) to the peak (002) of IL-RGO, a reflection crossover could be presented.

Since the content of IL-RGO is very low, the growth of ZIF-8 nanocrystals that occurred on the IL-RGO surfaces cannot be found by SEM and XRD. In order to further study the interaction between IL-RGO and ZIF-8, FTIR and micro Raman spectroscopy were carried out. Raman spectra are shown in Figure 2(b) for which IL-RGO has two feature peaks at 1354 and 1586 cm^{-1} associated with the G and D bands, respectively. The G band contributes to the vibration of graphitic (sp^2 carbon) lattice while the D band is related to the defects and disordered regions of the lattice caused by the oxidation reaction. Raman shifts of ZIF-8 at 686, 1144, 1183, 1459, and 1405 cm^{-1} are assigned to the vibrational modes of the Hmim ligand [34–36]. It is clear that the Raman shifts of both IL-RGO and ZIF-8 are presented in IL-RGO/ZIF-8 nanocomposites; furthermore, the intensity of feature peak 1586 cm^{-1} associated with the G band of RGO becomes stronger with the increase of IL-RGO in

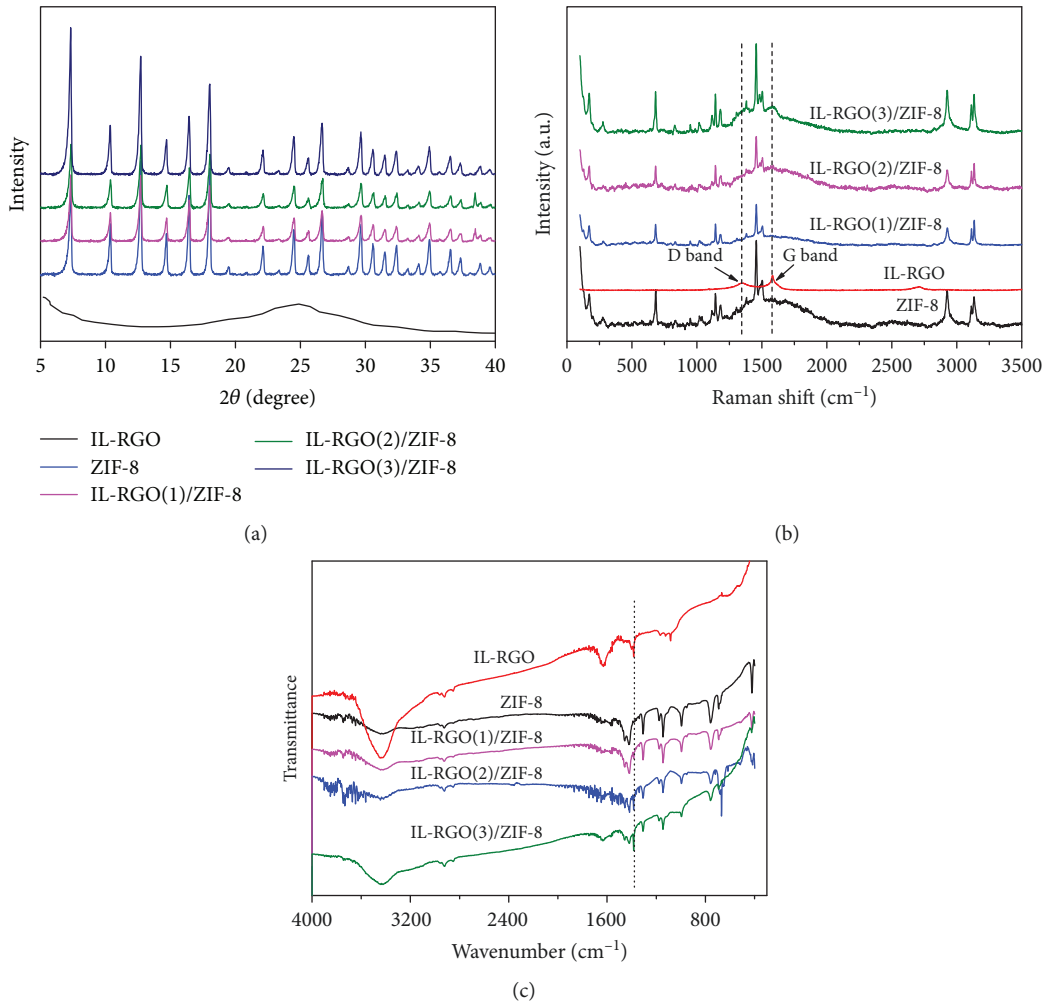

Figure 2: (a) XRD patterns, (b) Raman spectra, and (c) FTIR spectra of ZIF-8, IL-RGO, and IL-RGO/ZIF-8 nanocomposites.

the IL-RGO/ZIF-8 nanocomposites. It suggests that ZIF-8 is anchored on the IL-RGO.

The FTIR spectra of the nanocomposites are shown in Figure 2(c). The major absorption peaks are clear at 3428 cm^{-1} (O–H), at 1760 cm^{-1} (C=O), at 1650 cm^{-1} (skeletal C=C), at 1244 cm^{-1} (C–OH), and at 1080 cm^{-1} (C–O) [37–39]. The FTIR spectrum of ZIF-8 shows the vibrational modes of the Hmim ligand. The peaks at 3135 cm^{-1}, 2929 cm^{-1}, 1558 cm^{-1}, and 421 cm^{-1} are related to the aromatic and the aliphatic C–H, C=N, and Zn–N, respectively [40, 41]. The FTIR spectrum of the nanocomposites displays the same features to XRD as the ZIF-8 spectrum overwhelmed the peaks of IL-RGO due to the low loading content of IL-RGO. However, the absorption peak at 1382 cm^{-1} of IL-RGO is enhanced with the increase of IL-RGO in the IL-RGO/ZIF-8 nanocomposites, which is in agreement with the Raman results.

Nitrogen adsorption-desorption isotherms of pure ZIF-8 and IL-RGO/ZIF-8 composites are shown in Figure 3. The N_2 adsorption of the pure ZIF-8 and IL-RGO/ZIF-8 composites exhibited type I profile, which indicated that both ZIF-8 and IL-RGO/ZIF-8 composites were dominated by microporous structure. The surface area of pure ZIF-8, IL-RGO(1)/ZIF-8, IL-RGO(2)/ZIF-8, and IL-RGO(3)/ZIF-8 is 1067.5 m^2/g, 979.8 m^2/g, 1030.4 m^2/g, and 914.6 m^2/g, respectively. Among the IL-RGO/ZIF-8 nanocomposites, IL-RGO(2)/ZIF-8 owns the largest microporous surface area which is only a little smaller than that of pure ZIF-8. According to the electrochemical response of DA for the nanocomposites as shown in Figure 4, IL-RGO(2)/ZIF-8 has the best detective performance with the strongest current peak. The microporous surface area could play an important role on improving the electrochemical capability. Although pure ZIF-8 has the largest surface area with 1067.5 m^2/g, the electrochemical detection ability of pure ZIF-8 is worse than that of IL-RGO/ZIF-8 composites due to its poor electrical conductivity.

3.2. Electrochemical Response of DA for Different Electrodes. The electrochemical behavior of DA at different electrodes was studied in the PBS (0.1 M, pH 7.0) using the CV method in order to evaluate the electrocatalytic activity of the IL-RGO/ZIF-8 nanocomposites as shown in Figure 4. It can be seen that DA undergoes a good reversible oxidation-reduction reaction at the bare GCE and IL-RGO/GCE. Anodic and cathodic peaks of bare GCE are stronger than

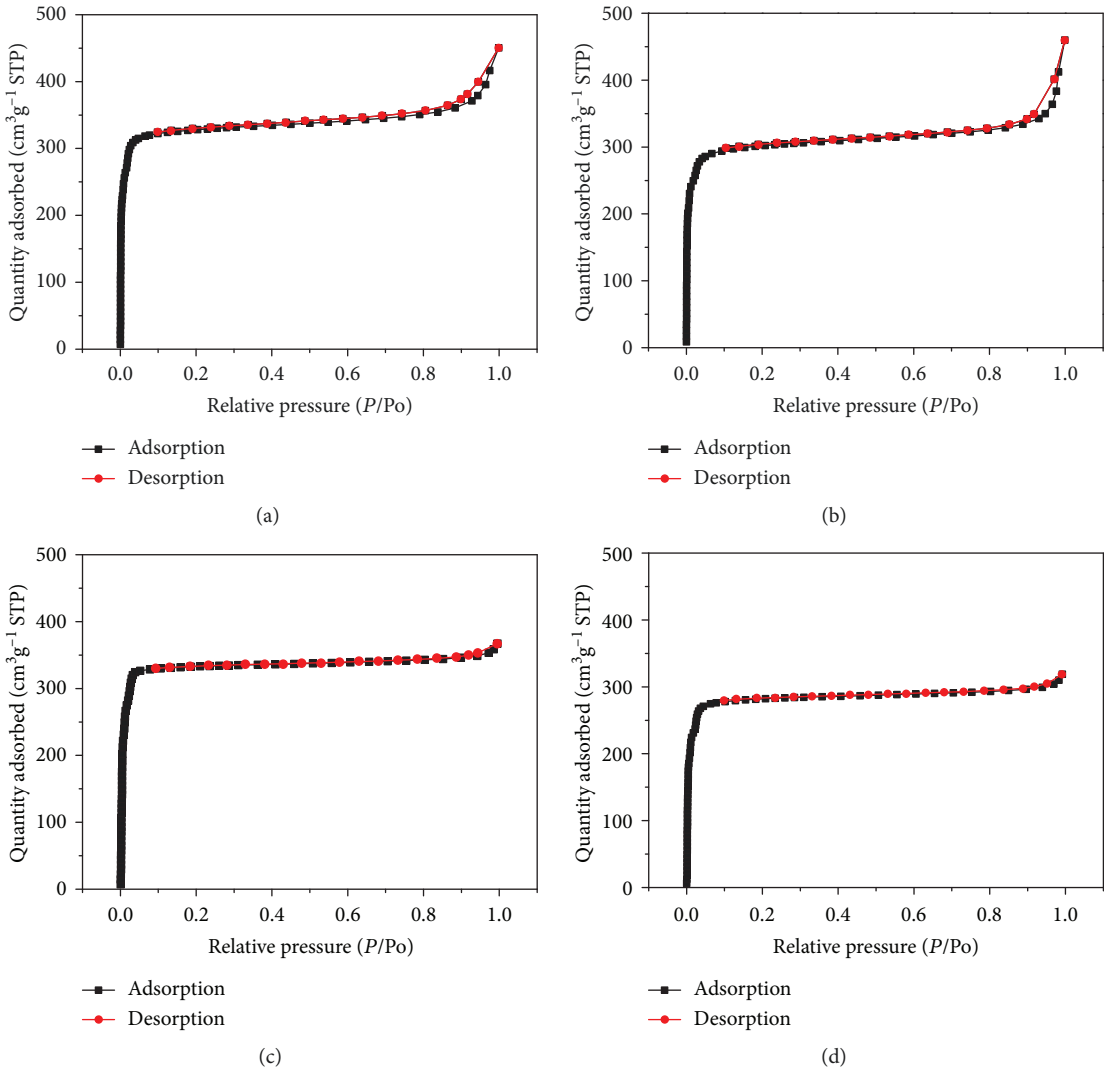

Figure 3: N_2 adsorption-desorption isotherms for (a) ZIF-8, (b) IL-RGO(1)/ZIF-8, (c) IL-RGO(2)/ZIF-8, and (d) IL-RGO(3)/ZIF-8.

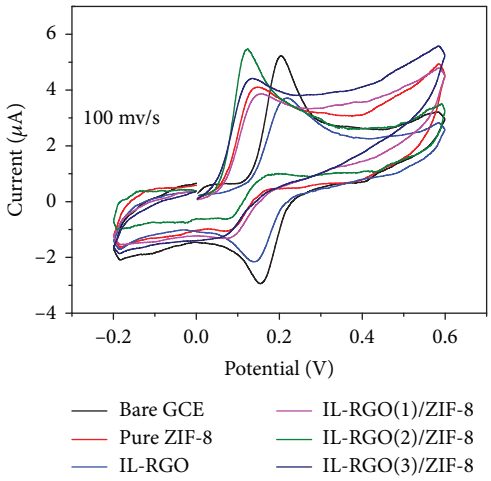

Figure 4: CV curves of bare GCE, ZIF-8/GCE, IL-RGO/GCE, and IL-RGO/ZIF-8/GCE in 0.1 M PBS solution (pH 7.0) containing 1.0×10^{-4} M DA.

those of IL-RGO/GCE, indicating a possible repulsive interaction between DA and IL-RGO. When ZIF-8 is introduced in electrodes, the electrochemical reaction of DA becomes highly irreversible; in addition, the overpotential is significantly decreased. It is very important that IL-RGO/ZIF-8/GCE shows the strongest current peak, which is associated with the synergistic effect from large surface areas of ZIF-8 and good electrical conductivity of IL-RGO. The content of IL-RGO in the composite influenced the electrochemical capability of modified electrode due to the repulsive effect of IL-RGO, and the 0.10 wt% was identified the best proportion of IL-RGO. This kind of composite was employed for the following determination of DA.

3.3. Impedance and Transport Behavior of IL-RGO/ZIF-8 Nanocomposites. Electrochemical impedance spectroscopy (EIS) is an effective tool for probing the interfacial behavior of modified electrodes; furthermore, it is also usually employed for understanding the chemical transformation associated with conductive supports [42]. Figure 5(a) shows EIS results of the bare GCE, ZIF-8/GCE, IL-RGO/GCE, and

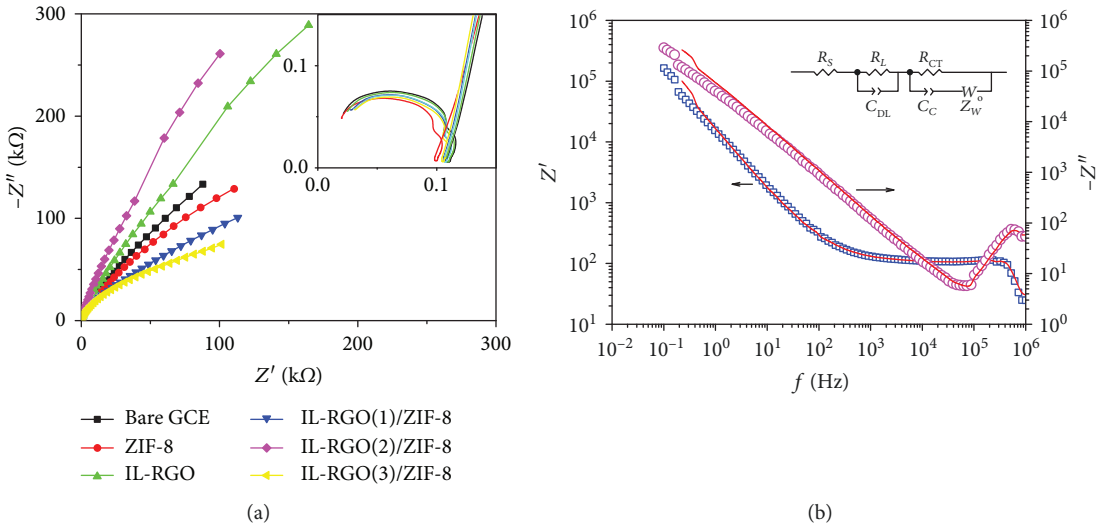

Figure 5: (a) Nyquist plots of the bare GCE, ZIF-8/GCE, IL-RGO/GCE, and IL-RGO/ZIF-8 with different contents of IL-RGO-modified GCEs in the presence of 0.1 M PBS solution (pH 7.0) containing 1.0×10^{-4} M DA; inset: semicircles at high frequency. (b) Frequency as a function of the real part and imaginary part of impedance of IL-RGO(2)/ZIF-8/GCE (the diamond is the real part of the impedance and the pink circle is the imaginary part of the impedance). Inset: the equivalent circuit of the IL-RGO/ZIF-8/GCE electrode in PBS solid solution. The red solid lines were fitted by the inset equivalent circuit.

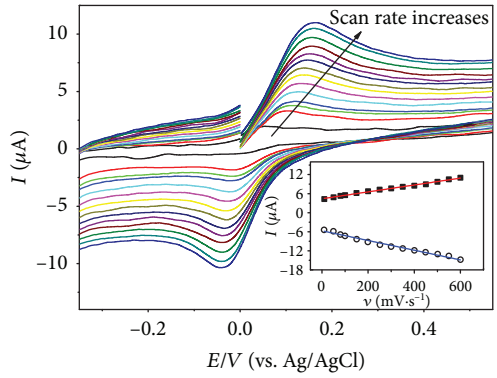

Figure 6: CV curves of IL-RGO(2)/ZIF-8/GCE in 0.1 M PBS solution (pH 7.0) containing 1.0×10^{-4} M DA at different scan rates: 10, 50, 80, 100, 150, 200, 250, 300, 350, 400, 450, 500, 550, and 600 mV·s^{-1}. Inset: plots of the anodic and cathodic peak currents (I_{pa} and I_{pc}) vs. the scan rate.

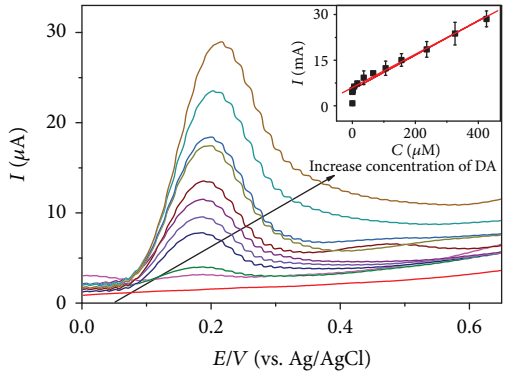

Figure 7: DPV curve for different concentrations of DA (from bottom to top: 0, 0.01, 0.1, 1, 5, 10, 30, 50, 70, 90, and 100 μM) on IL-RGO(2)/ZIF-8/GCE in 0.1 M PBS solution with pH 7.0 (scan rate: 100 mV·s^{-1}). Inset: the linear calibration plots of peak current (I_{pa}) versus the concentration of DA.

different contents of IL-RGO/ZIF-8/GCE in the presence of 0.1 M PBS solution (pH 7.0) containing 1.0×10^{-4} M DA at a frequency range from 0.01 Hz to 1 MHz. The typical Nyquist plot includes a semicircle at higher frequencies related to the electron transfer-limited process and a linear part at lower frequencies corresponding to the diffusion-limited processes. In this system, an addition semicircle can be found in the high frequency, as shown in the inset of Figure 5(a). In order to present the impedance information in the whole probing frequency, the real part and imaginary part of impedance of IL-RGO(2)/ZIF-8/GCE are plotted in Figure 5(b); the corresponding equivalent circuit is shown in the inset of Figure 5(b). The fitting curves (solid lines in Figure 5(b)) based on the equivalent circuit match the measurement results well, indicating that the circuit is reasonable to describe the electrochemical process. For the equivalent circuit, R_S is the bulk solution resistance of the electrolyte, C_{DL} is the electrical double layer capacitor of the system, R_L is the leakage resistance, C_C is the interfacial contact capacitance, R_{CT} is the ionic charge transfer resistance of DA on electrodes, and Z_W is the Warburg impedance. According to the fitting results, R_S and R_L of all plots are the same about 17.5 Ω and 81.5 Ω, respectively, while the magnitude of C_{DL} is about ~10^{-11} F slightly dependent on the modifiers on the electrodes. It suggests that the electrolyte and interface between solution and electrodes remain unchanged with different modifiers (IL-RGO, ZIF-8, and IL-RGO/ZIF-8). R_{CT} plays a key role on the performance of electrodes. It exhibits the electron transfer kinetics of the redox probe at the electrode interface. IL-RGO(2)/ZIF-8/GCE shows a low electron transfer resistance about 141700, which is lower than that of bare GEC and ZIF-8/GEC and IL-RGO(1)/ZIF-8/GCE. The

Table 1: Comparison of analytical performances for DA at different modified electrodes.

Modifier	Method	Linear ranges (μM)	Detection limits (μM)	Reference
GO	DPV	0.15-1	0.27	[45]
Polypyrrole@RGO	DPV	0.06-8	6×10^{-3}	[46]
Fe_3O_4/RGO	DPV	0.04-1.6	0.08	[47]
Fe_3O_4@ZIF-8/RGO	DPV	2×10^{-4}-10	6.67×10^{-4}	[48]
Au NPs@RGO	DPV	0.5-20	0.13	[49]
Cu(tpa)-EGR	DPV	1-50	0.21	[50]
IL-RGO/ZIF-8	DPV	0.1-100	0.035	This work

low resistance of IL-RGO(2)/ZIF-8/GCE is attributed to the synergistic effect of ZIF-8 and IL-RGO that enhanced the rate of electron transfer, which is agreement with the CV results.

The dynamic and transport characteristic of IL-RGO(2)/ZIF-8/GCE was determined by CV curves with different scan rates on the oxidation of 0.1 mM DA. The oxidation and reduction peak currents of DA, as shown in Figure 6, exhibit ideal linear relationship towards the scan rate (v) in the range from 10 to 600 mV·s^{-1}. It suggests that the electrochemical reaction of DA on IL-RGO(2)/ZIF-8/GCE is an adsorption-controlled process. The linear relationship is $I_{pa}\,(\mu A) = 4.3828 + 0.0108\,v$ (mV·s^{-1}) ($R^2 = 0.993$) and $I_{pc}\,(\mu A) = -5.6935 - 0.0153\,v$ (mV·s^{-1}) ($R^2 = 0.992$). The anodic peak shifts towards more positive while the cathodic peak shifts towards more negative with the increase of scan rate, which indicates a reversible electron transfer for DA. The number of electron transfer (n) of the redox process of DA can be estimated [43]:

$$I_p = \frac{n^2 F^2 A \Gamma v}{4RT} = \frac{nFQv}{4RT}, \quad (1)$$

where I_p is the peak current, F is the Faraday constant (96485 C ·mol^{-1}), A is the electrode surface area (m^2), Γ is the surface concentration of the electroactive substance (mol m^{-2}), v is the scanning rate (V s^{-1}), R is the gas molar constant (8.314 J mol^{-1} K^{-1}), T is the absolute temperature (298 K in this process), and $Q = nFA\Gamma$ is the peak area (calculated by the charges) (C). n is evaluated 1.95 from the relation between I_p and v. Further, the value of Γ can be obtained as 8.6×10^{-6} mol m^{-2}, which indicates that IL-RGO(2)/ZIF-8 provides a three-dimensional structure for the effective adsorption of DA. The increased concentration of DA on the electrode surface gives rise to the improvement of the sensitivity. As mentioned above, the redox reaction of DA includes two electrons and two protons process as suggested:

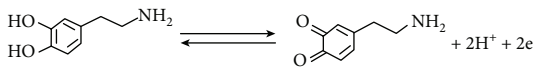

3.4. Determination of DA. DPV was employed to evaluate the electrochemical detection performance of IL-RGO(2)/ZIF-8/GCE towards DA due to its higher analytical signal than that of CV. It can be seen from Figure 7 that the peak current of DA increases linearly with the concentration of DA in the range from 1.0×10^{-7} M to 1.0×10^{-4} M. A linear relationship can be obtained: $I_p\,(\mu A) = 5.3328 + 0.0567\,C\,(\mu M)$ ($R^2 = 0.998$). The limit of detection (LOD) can be calculated 3.5×10^{-8} M ($S/N = 3$), and the sensitivity is 0.0567 μA μM^{-1}. The comparison of the performance of IL-RGO/ZIF-8 nanocomposite with other materials for sensing DA is listed in Table 1. It is clear that IL-RGO/ZIF-8 nanocomposite has a low detection limit and wide linear range. The excellent electrochemical analytical performance could be attributed to the synergistic effect of IL-RGO and ZIF-8. ZIF-8 has order pore structure and large surface area while IL-RGO has good electrical conductivity. Both electron transfer and mass transfer could be enhanced in the composite of IL-RGO and ZIF-8. Furthermore, the growth of ZIF-8 on IL-RGO prevents the aggregation of graphene, which promotes its electroanalysis performance [44].

3.5. Reproducibility and Stability of the Electrochemical Sensor. Six paralleled electrodes were prepared with the same condition for evaluating the reproducibility of IL-RGO(2)/ZIF-8/GCE by detecting current signal in PBS buffer with 1.0×10^{-4} M DA. The relative standard deviation (RSD) of the electrodes is 2.4%. The stability of IL-RGO(2)/-ZIF-8/GCE was verified by intermittently testing current signal of 1.0×10^{-4} M DA every three days with 5 cycles. After each testing, the electrodes were stored in a refrigerator at 4°C. The RSD for the testing is 4.7%. It indicates that good stability and reproducibility can be obtained for electrochemical detection by the prepared electrodes.

4. Conclusions

A novel nanocomposite IL-RGO/ZIF-8 was prepared by the in situ growth of ZIF-8 on a small quantity of IL-RGO template. Both electron transfer and mass transfer were enhanced due to the combination of the great electric conductivity for IL-RGO and the large surface area and order pore structure for ZIF-8. IL-RGO(2)/ZIF-8/GCE shows very good sensitivity for the determination of DA. In addition, the electrochemical sensor displays great reproducibility and stability. As a result, it is considered that the IL-RGO/ZIF-8 nanocomposite has excellent electrochemical performance and potential application as a novel electrochemical detection platform.

Data Availability

The data used to support the findings of this study are included within the article.

Conflicts of Interest

The authors declare that there is no conflict of interest regarding the publication of this paper.

Acknowledgments

Funding from the National Natural Science Foundation of China (21671046, 21502028, and 21601038) and the Guangxi Natural Science Foundation of China (2017GXNSFGA198004 and 2018GXNSFAA281220) is acknowledged. The authors appreciate Dr. Huahong Zou for his useful discussion and kind help.

References

[1] L. Wu, L. Y. Feng, J. S. Ren, and X. G. Qu, "Electrochemical detection of dopamine using porphyrin-functionalized graphene," *Biosensors and Bioelectronics*, vol. 34, no. 1, pp. 57–62, 2012.

[2] W. X. Zhang, J. Z. Zheng, J. G. Shi et al., "Nafion covered core–shell structured Fe_3O_4@graphene nanospheres modified electrode for highly selective detection of dopamine," *Analytica Chimica Acta*, vol. 853, pp. 285–290, 2015.

[3] S. E. Hyman and R. C. Malenka, "Addiction and the brain: the neurobiology of compulsion and its persistence," *Nature Reviews. Neuroscience*, vol. 2, no. 10, pp. 695–703, 2001.

[4] W. Gao, L. Qi, Z. Liu, S. Majeed, S. A. Kitte, and G. Xu, "Efficient lucigenin/thiourea dioxide chemiluminescence system and its application for selective and sensitive dopamine detection," *Sensors and Actuators B: Chemical*, vol. 238, pp. 468–472, 2017.

[5] K. T. Ngo, E. L. Varner, A. C. Michael, and S. G. Weber, "Monitoring dopamine responses to potassium ion and nomifensine by in vivo microdialysis with online liquid chromatography at one-minute resolution," *ACS Chemical Neuroscience*, vol. 8, no. 2, pp. 329–338, 2017.

[6] S. Janku, M. Komendova, and J. Urban, "Development of an online solid-phase extraction with liquid chromatography method based on polymer monoliths for the determination of dopamine," *Journal of Separation Science*, vol. 39, no. 21, pp. 4107–4115, 2016.

[7] H. F. Fang, M. L. Pajski, A. E. Ross, and B. J. Venton, "Quantitation of dopamine, serotonin and adenosine content in a tissue punch from a brain slice using capillary electrophoresis with fast-scan cyclic voltammetry detection," *Analytical Methods*, vol. 5, no. 11, pp. 2704–2711, 2013.

[8] J. J. Zhao, L. M. Zhao, C. Q. Lan, and S. L. Zhao, "Graphene quantum dots as effective probes for label-free fluorescence detection of dopamine," *Sensors and Actuators B: Chemical*, vol. 223, pp. 246–251, 2016.

[9] Q. Y. Zhao, F. F. Zhang, J. F. Xia et al., "Self-assembled ionic liquid-phosphomolybdic acid/reduced graphene oxide composite modified electrode for sensitive determination of dopamine," *ECS Journal of Solid State Science and Technology*, vol. 6, no. 6, pp. M3014–M3018, 2017.

[10] W. Liu and X. B. Yin, "Metal–organic frameworks for electrochemical applications," *TrAC Trends in Analytical Chemistry*, vol. 75, pp. 86–96, 2016.

[11] L. T. Liu, Y. L. Zhou, S. Liu, and M. T. Xu, "The applications of metal–organic frameworks in electrochemical sensors," *ChemElectroChem*, vol. 5, no. 1, pp. 6–19, 2018.

[12] W. J. Ma, Q. Jiang, P. Yu, L. F. Yang, and L. Q. Mao, "Zeolitic imidazolate framework-based electrochemical biosensor for in vivo electrochemical measurements," *Analytical Chemistry*, vol. 85, no. 15, pp. 7550–7557, 2013.

[13] J. Yang, H. L. Ye, F. Q. Zhao, and B. Z. Zeng, "A novel Cu_xO nanoparticles@ZIF-8 composite derived from core–shell metal–organic frameworks for highly selective electrochemical sensing of hydrogen peroxide," *ACS Applied Materials & Interfaces*, vol. 8, no. 31, pp. 20407–20414, 2016.

[14] H. R. Moon, D. W. Lim, and M. P. Suh, "Fabrication of metal nanoparticles in metal-organic frameworks," *Chemical Society Reviews*, vol. 42, no. 4, pp. 1807–1824, 2013.

[15] Z. Zhang, H. T. H. Nguyen, S. A. Miller, and S. M. Cohen, "polyMOFs: a class of interconvertible polymer-metal-organic-framework hybrid materials," *Angewandte Chemie International Edition*, vol. 54, no. 21, pp. 6152–6157, 2015.

[16] Z. H. Xiang, Z. Hu, D. P. Cao et al., "Metal–organic frameworks with incorporated carbon nanotubes: improving carbon dioxide and methane storage capacities by lithium doping," *Angewandte Chemie International Edition*, vol. 50, no. 2, pp. 491–494, 2011.

[17] Y. F. Jin, C. Y. Ge, X. B. Li, M. Zhang, and G. R. Xu, "A sensitive electrochemical sensor based on ZIF-8–acetylene black–chitosan nanocomposites for rutin detection," *RSC Advances*, vol. 8, no. 57, pp. 32740–32746, 2018.

[18] J. F. Xia, X. Y. Cao, Z. H. Wang et al., "Molecularly imprinted electrochemical biosensor based on chitosan/ionic liquid–graphene composites modified electrode for determination of bovine serum albumin," *Sensors and Actuators B: Chemical*, vol. 225, pp. 305–311, 2016.

[19] P. Bollella, G. Fusco, C. Tortolini et al., "Beyond graphene: electrochemical sensors and biosensors for biomarkers detection," *Biosensors and Bioelectronics*, vol. 89, Part 1, pp. 152–166, 2017.

[20] Y. Wang, C. Hou, Y. Zhang, F. He, M. Liu, and X. Li, "Preparation of graphene nano-sheet bonded pda/mof microcapsules with immobilized glucose oxidase as a mimetic multi-enzyme system for electrochemical sensing of glucose," *Journal of Materials Chemistry B*, vol. 4, no. 21, pp. 3695–3702, 2016.

[21] D. Kim, D. W. Kim, W. G. Hong, and A. Coskun, "Graphene/-ZIF-8 composites with tunable hierarchical porosity and electrical conductivity," *Journal of Materials Chemistry A*, vol. 4, no. 20, pp. 7710–7717, 2016.

[22] G. G. Yu, J. F. Xia, F. F. Zhang, and Z. H. Wang, "Hierarchical and hybrid RGO/ZIF-8 nanocomposite as electrochemical sensor for ultrasensitive determination of dopamine," *Journal of Electroanalytical Chemistry*, vol. 801, pp. 496–502, 2017.

[23] D. Li, M. B. Muller, S. Gilje, R. B. Kaner, and G. G. Wallace, "Processable aqueous dispersions of graphene nanosheets," *Nature Nanotechnology*, vol. 3, no. 2, pp. 101–105, 2008.

[24] H. Yang, C. Shan, F. Li, D. Han, Q. Zhang, and L. Niu, "Covalent functionalization of polydisperse chemically-converted graphene sheets with amine-terminated ionic liquid," *Chemical Communications*, vol. 26, no. 26, pp. 3880–3882, 2009.

[25] D. Wei and A. Ivaska, "Applications of ionic liquids in electrochemical sensors," *Analytica Chimica Acta*, vol. 607, no. 2, pp. 126–135, 2008.

[26] C. Shan, H. Yang, D. Han, Q. Zhang, A. Ivaska, and L. Niu, "Electrochemical determination of NADH and ethanol based on ionic liquid-functionalized graphene," *Biosensors and Bioelectronics*, vol. 25, no. 6, pp. 1504–1508, 2010.

[27] J. Peng, C. Hou, and X. Hu, "Determination of metronidazole in pharmaceutical dosage forms based on reduction at graphene and ionic liquid composite film modified electrode," *Sensors and Actuators B: Chemical*, vol. 169, pp. 81–87, 2012.

[28] Q. G. Shao, J. Tang, Y. X. Lin et al., "Ionic liquid modified graphene for supercapacitors with high rate capability," *Electrochimica Acta*, vol. 176, pp. 1441–1446, 2015.

[29] S. Tanaka, K. Kida, M. Okita, Y. Ito, and Y. Miyake, "Size-controlled synthesis of zeolitic imidazolate framework-8 (ZIF-8) crystals in an aqueous system at room temperature," *Chemistry Letters*, vol. 41, no. 10, pp. 1337–1339, 2012.

[30] K. S. Park, Z. Ni, A. P. Cote et al., "Exceptional chemical and thermal stability of zeolitic imidazolate frameworks," *Proceedings of the National Academy of Sciences of the United States of America*, vol. 103, no. 27, pp. 10186–10191, 2006.

[31] J. Cravillon, R. Nayuk, S. Springer, A. Feldhoff, K. Huber, and M. Wiebcke, "Controlling zeolitic imidazolate framework nano- and microcrystal formation: insight into crystal growth by time-resolved in situ static light scattering," *Chemistry of Materials*, vol. 23, no. 8, pp. 2130–2141, 2011.

[32] M. He, J. Yao, Q. Liu, K. Wang, F. Chen, and H. Wang, "Facile synthesis of zeolitic imidazolate framework-8 from a concentrated aqueous solution," *Microporous and Mesoporous Materials*, vol. 184, pp. 55–60, 2014.

[33] H. Chen, L. Wang, J. Yang, and R. T. Yang, "Investigation on hydrogenation of metal–organic frameworks HKUST-1, MIL-53, and ZIF-8 by hydrogen spillover," *Journal of Physical Chemistry C*, vol. 117, no. 15, pp. 7565–7576, 2013.

[34] R. Kumar, K. Jayaramulu, T. K. Maji, and C. N. R. Rao, "Hybrid nanocomposites of ZIF-8 with graphene oxide exhibiting tunable morphology, significant CO_2 uptake and other novel properties," *Chemical Communications*, vol. 49, no. 43, pp. 4947–4949, 2013.

[35] C. Petit and T. J. Bandosz, "Synthesis, characterization, and ammonia adsorption properties of mesoporous metal–organic framework (MIL(Fe))–graphite oxide composites: exploring the limits of materials fabrication," *Advanced Functional Materials*, vol. 21, no. 11, pp. 2108–2117, 2011.

[36] S. Luanwuthia, A. Krittayavathananona, P. Srimuka, and M. Sawangphruk, "*In situ* synthesis of permselective zeolitic imidazolate framework-8/graphene oxide composites: rotating disk electrode and Langmuir adsorption isotherm," *RSC Advances*, vol. 5, no. 58, pp. 46617–46623, 2015.

[37] D. C. Marcano, D. V. Kosynkin, J. M. Berlin et al., "Improved synthesis of graphene oxide," *ACS Nano*, vol. 4, no. 8, pp. 4806–4814, 2010.

[38] Y. Sanguansak, P. Srimuk, A. Krittayavathananon et al., "Permselective properties of graphene oxide and reduced graphene oxide electrodes," *Carbon*, vol. 68, pp. 662–669, 2014.

[39] T. Rattana, S. Chaiyakun, N. Witit-anun et al., "Preparation and characterization of graphene oxide nanosheets," *Procedia Engineering*, vol. 32, pp. 759–764, 2012.

[40] Y. Hu, H. Kazemian, S. Rohani, Y. Huang, and Y. Song, "*In situ* high pressure study of ZIF-8 by FTIR spectroscopy," *Chemical Communications*, vol. 47, no. 47, pp. 12694–12696, 2011.

[41] J. Yao, R. Chen, K. Wang, and H. Wang, "Direct synthesis of zeolitic imidazolate framework-8/chitosan composites in chitosan hydrogels," *Microporous and Mesoporous Materials*, vol. 165, pp. 200–204, 2013.

[42] M. I. Prodromidis, "Impedimetric immunosensors-a review," *Electrochimica Acta*, vol. 55, no. 14, pp. 4227–4233, 2010.

[43] E. Laviron, "General expression of the linear potential sweep voltammogram in the case of diffusionless electrochemical systems," *Journal of Electroanalytical Chemistry and Interfacial Electrochemistry*, vol. 101, no. 1, pp. 19–28, 1979.

[44] J. F. Xia, Z. H. Wang, F. Cai et al., "An electrochemical sensor for the sensitive detection of rutin based on a novel composite of activated silica gel and graphene," *RSC Advances*, vol. 5, no. 49, pp. 39131–39137, 2015.

[45] F. Gao, X. L. Cai, X. Wang et al., "Highly sensitive and selective detection of dopamine in the presence of ascorbic acid at graphene oxide modified electrode," *Sensors and Actuators B: Chemical*, vol. 186, pp. 380–387, 2013.

[46] T. Qian, S. S. Wu, and J. Shen, "Facilely prepared polypyrrole-reduced graphite oxide core–shell microspheres with high dispersibility for electrochemical detection of dopamine," *Chemical Communications*, vol. 49, no. 41, pp. 4610–4612, 2013.

[47] H. Teymourian, A. Salimi, and S. Khezrian, "Fe_3O_4 magnetic nanoparticles/reduced graphene oxide nanosheets as a novel electrochemical and bioeletrochemical sensing platform," *Biosensors & Bioelectronics*, vol. 49, pp. 1–8, 2013.

[48] Y. Wang, Y. Zhang, C. Hou, and M. Z. Liu, "Magnetic Fe_3O_4@MOFs decorated graphene nanocomposites as novel electrochemical sensor for ultrasensitive detection of dopamine," *RSC Advances*, vol. 5, no. 119, pp. 98260–98268, 2015.

[49] T. Chen, L. Tang, F. Yang et al., "Electrochemical determination of dopamine by a reduced graphene oxide-gold nanoparticle-modified glassy carbon electrode," *Analytical Letters*, vol. 49, no. 14, pp. 2223–2233, 2016.

[50] X. Wang, Q. X. Wang, Q. H. Wang et al., "Highly dispersible and stable copper terephthalate metal–organic framework–graphene oxide nanocomposite for an electrochemical sensing application," *ACS Applied Materials & Interfaces*, vol. 6, no. 14, pp. 11573–11580, 2014.